A Soft Modular Manipulator for Minimally Invasive Surgery: Design and Characterization of a Single Module

Tommaso Ranzani, Matteo Cianchetti, *Member, IEEE*, Giada Gerboni, *Member, IEEE*,
Iris De Falco, and Arianna Menciassi, *Senior Member, IEEE*

***Abstract*—This paper presents the concept design of a modular soft manipulator for minimally invasive surgery. Unlike traditional surgical manipulators based on metallic steerable needles, tendon-driven mechanisms, or articulated motorized links, we combine flexible fluidic actuators to obtain multidirectional bending and elongation with a variable stiffness mechanism based on granular jamming. The idea is to develop a manipulator based on a series of modules, each consisting of a silicone matrix with pneumatic chambers for 3-D motion, and one central channel for the integration of granular-jamming-based stiffening mechanism. A bellows-shaped braided structure is used to contain the lateral expansion of the flexible fluidic actuator and to increase its motion range. In this paper, the design and experimental characterization of a single module composed of such a manipulator is presented. Possible applications of the manipulator in the surgical field are discussed.**

***Index Terms*—Fluidic actuation, granular jamming, minimally invasive surgery (MIS), soft robot, variable stiffness.**

I. INTRODUCTION

INCREASING interest in minimally invasive surgical procedures has led to the development of surgical instrumentation that can reach the surgical target from multiple small entrances (laparoscopy), or several tools can be inserted from a single access (single-port laparoscopy) or from natural orifices as in natural orifice translumenal endoscopic surgery (NOTES) [1]. All three approaches fall under the definition of minimal access surgery (MAS), in which generally rigid or semirigid tools are used to reach the target area. However, the passage toward the surgical target can often be obstructed by other organs or anatomical structures. This, together with the reduced dexterity of the instruments, represents an important limitation in the execution of many surgical procedures.

MAS can benefit from the introduction of robotic technologies; for example, in terms of restoring the intuitiveness of the procedure and providing additional tip dexterity, as demonstrated by the success of the DaVinci surgical robot [2]. This robot mimics the structure of a standard laparoscopic instrument, which is based on a rigid long shaft, and the surgical tool is placed on the tip and oriented with an articulated wrist.

Articulated flexible instruments are highly dexterous in reaching a specific body region from a remote access and thus have been proposed for operating in the heart [3], throat [4], [5], brain [6], or abdominal organs, through a single-port access [7] or a natural orifice [8].

In order to carry out a surgical intervention, conventional minimally invasive surgery (MIS) often requires the use of multiple dedicated instruments such as dissectors, grippers, retractors, and cameras [9]. In fact, even a single and simple surgical task requires the simultaneous use of two or more of the above instruments. The integration of multiple instruments or functionalities onboard the same tool introduces technical challenges, particularly when surgical retraction is needed. Retraction is necessary in order to expose the surgical target when it is located below an organ or collapsed tissues, which need to be lifted or shifted. In addition, this action often requires the application of considerable forces [10].

Current devices for organ retraction in abdominal surgery are simple assistive laparoscopic devices such as the Cinch Organ Retractor (Aesculap, Inc.), the T'LIFT laparoscopic tissue retraction system (VECTEC, France), and the Endograb (Virtual Ports, Ltd.) [11], which mainly involve organ piercing by means of a hook, or the Endoloop Ligature device (Ethicon, Endo-Surgery, Johnson&Johnson Medical), which uses a looped ligature inserted into a plastic tube to reach the organ that needs to be retracted. At the research level, there have been a few attempts to reduce the invasiveness of organ retraction using magnetic systems [12]–[15] or a hybrid system of magnetic anchoring and chemical adhesive film [16].

Since retraction requires a safe and compliant interaction with tissues and organs, the emerging field of soft robotics offers promising alternatives to current systems. Indeed, due to the compliance of the materials involved (e.g., elastomers), soft robots have been exploited to safely touch or interact with delicate objects [17], [18].

In previous works, the authors have discussed how soft robotics technologies can provide valuable support for the development of highly dexterous compliant instrumentation for both retraction as well as for approaching and grasping organs [19]. Examples of soft and shrinkable instruments for

Manuscript received February 13, 2015; revised August 18, 2015 and September 16, 2015; accepted December 6, 2015. This paper was recommended for publication by Associate Editor N. Simaan and Editor B. J. Nelson upon evaluation of the reviewers' comments. This work was supported by the STIFF-FLOP project from the European Community Seventh Framework Program under Grant 287728.

The authors are with The BioRobotics Institute, Scuola Superiore Sant'Anna, Pontedera 56025, Italy (e-mail: tranzani@seas.harvard.edu; matteo.cianchetti@sssup.it; giada.gerboni@sssup.it; iris.defalco@sssup.it; arianna.menciassi@sssup.it).

This paper has supplementary downloadable material available at http://ieeexplore.ieee.org.

Color versions of one or more of the figures in this paper are available online at http://ieeexplore.ieee.org.

Digital Object Identifier 10.1109/TRO.2015.2507160

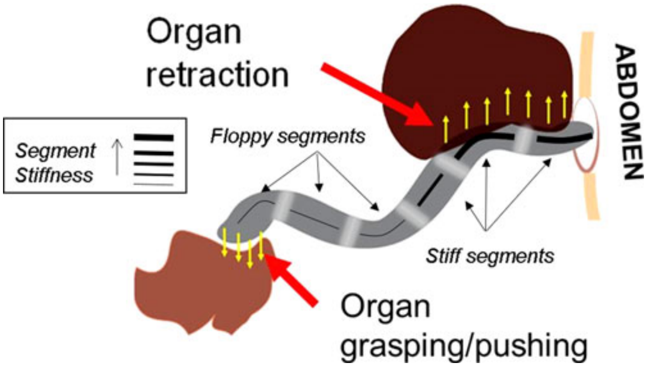

Fig. 1. Envisaged surgical scenario with a manipulator composed of multiple modules interconnected. The manipulator is able to pass through a single port access and to retract/push organs and tissues with different modules along the device exploiting selective stiffening of its segments.

self-propulsion in diagnosis and for basic surgical applications in the gastrointestinal tract are reported in [20] and [21].

For more complicated tasks such as retraction or grasping, the manipulator also needs to be able to modulate its stiffness and thus actively exert a force when necessary; for example, for lifting and supporting an organ. The need for stiffness control in robots presenting a continuum or soft structure has been addressed in [22], where a stiffness controller based on the kinematics of robots is presented. A step further is proposed in [23], where the issue of monitoring the contact with a compliant environment is addressed.

Variable stiffness surgical robots have been proposed in [24]–[26]. Similar to the locking mechanisms of endoscopes, such systems are only used to freeze the shape of the instrument during surgery, but no active interaction with the body of the instrument with the surroundings is envisaged. Instead, a variable stiffness device offers the possibility of modulating the interaction and the force exerted against the surroundings. In addition if, for example, the manipulator has different levels of stiffness in various parts of its body, the same device can be also used for multiple tasks, as shown in Fig. 1.

In [27], the authors presented a soft bioinspired manipulator based on the design introduced in [28], focusing on the integration of two modules to increase the manipulator dexterity, and demonstrated manipulation of phantom organs exploiting selective stiffening to tune the interactions with them.

In this paper, the authors deepen the design and characterization of the single module that embodies the building block of such a soft, variable stiffness surgical robot. All the components of the module are detailed in terms of design, fabrication, and characterization. An integrated prototype of the module is extensively characterized in terms of dexterity, forces generated, and stiffening capabilities. The conceptual design of the entire manipulator is described in Section II, while Section III details all the components, their design, and integration in the single module manipulator. Section IV illustrates the experimental characterization of a single manipulator module. Tests and performance assessments are described in Section V and discussed in depth in Section VI.

II. MANIPULATOR STRUCTURE AND POSSIBLE SURGICAL SCENARIOS

The manipulator is composed of multiple modules following a homogenous modular structure, in which each module is identical in terms of design and functionalities [29]. There is an introduction to this device in [28], whereas the present paper provides, for the first time, a more detailed and comprehensive study and analysis of its properties, its manufacturing process, and a specific application. The robotic manipulator is inspired by the manipulation capabilities of the octopus arm, as devised in the STIFF-FLOP (STIFFness controllable Flexible & Learnable Manipulator for surgical OPerations) project [30]. The manipulator is designed to be particularly flexible during the elongation and bending of its structure, since it is squeezable in its passive state, but also capable of being stiff along its body. Each segment of the arm is able to apply forces, to perform multidirectional bending and elongation, and its stiffness can be tuned. This modular structure means that the whole length of the manipulator can be used to accomplish the surgical task, and not just to guide the end effector toward the surgical target. This functionality can be exploited, for example, by using a portion of the manipulator, such as the proximal part, to hold organs or biological structures (i.e., surgical retraction) and the remaining portion to carry out a different task, e.g., grasping [27]. In this scenario, selective stiffening of the different segments can be exploited to tune the compliance for it to interact with the surrounding biological structures. Other possible scenarios (not addressed in this paper) could include an instrument (such as an electro cautery hook or a simple grasper) fixed at the tip to carry out other specific surgical tasks or a wrist on the tip to provide additional dexterity, as proposed in [31].

III. DESIGN OF THE SINGLE MODULE

Each single module integrates all the basic functionalities of the entire STIFF-FLOP manipulator: active motion (i.e., omnidirectional bending and elongation) and stiffening. Flexible fluidic actuators (FFAs) are exploited for the bending and elongation of the module, while a granular-jamming-based stiffening mechanism is used for stiffness variation.

In this section, the actuation and the stiffening system design are presented and discussed.

A. *Design of the Active Motion System for Elongation and Bending*

FFAs were chosen to take advantage of elastomeric materials in order to make the module compliant and flexible [32], [33]. In addition, FFAs can provide high forces and do not require electrical connections and powering, thus facilitating their application in surgical robots and paving the way toward MRI compatibility [19], [33].

The actuator is composed of elastomeric material (Silicone 0050, Ecoflex, Smooth on Inc., Shore Hardness = 00–50, 100% linearized Tensile Modulus = 83 kPa). This material was selected due to its high flexibility, low hysteresis, and easy molding.

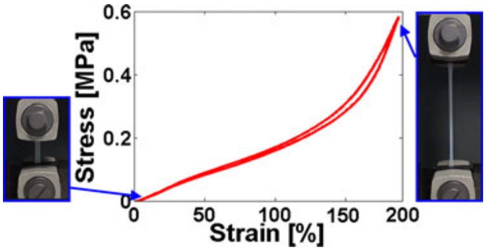

Fig. 2. Stress–strain test results of Silicone 0050 (Ecoflex, Smooth on Inc.). (Left inset) Initial length of the tested silicone sample. (Right inset) 200% deformation on the silicone sample.

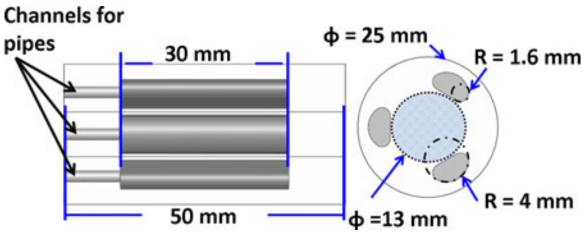

Fig. 3. Drawing of the silicone FFA and relevant dimensions. Lateral view (left) and top view (right) of the actuator. In the top view, the available space in the center of the actuator is highlighted.

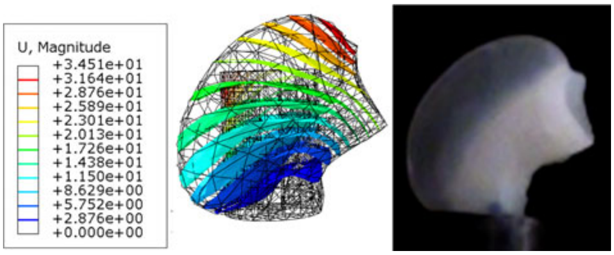

Fig. 4. Preliminary FEM results on the actuator deformation during a single-chamber inflation of 0.03 MPa, displacement is expressed in mm (left). The undeformed shape is overlapped in the background (middle). Experimental assessment on a fabricated FFA (right).

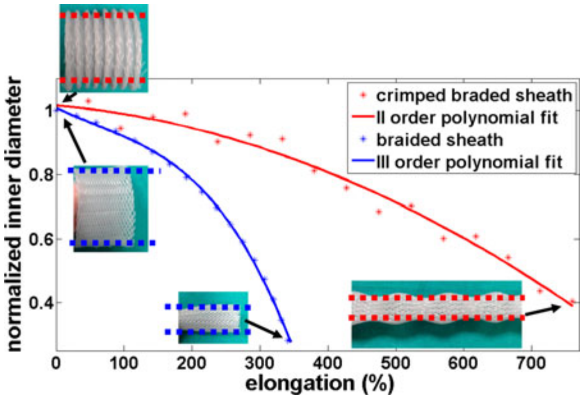

Fig. 5. Comparison between not crimped and crimped braided sheaths. The red curve represents the diameter variation in the crimped structure during elongation. The blue curve shows the diameter reduction in the case of a conventional braided sheath according to [41]. In the insets of the figure, the inner diameter change is highlighted with dashed lines.

The mechanical properties of the silicone were tested according to ISO 37:2005(E), and the stress–strain data are shown in Fig. 2. The curve in Fig. 2 represents the average of five cycles of loading/unloading of the silicone performed with an Instron 5900 Testing System. The maximum measured variability was ± 3.4 kPa and the hysteresis was 0.05 J. Data were fitted using a third-order reduced polynomial function (Yeoh model [34]) in order to derive the material model that was used for the finite-element analysis of the actuator.

The design of the FFAs comprises a silicone cylinder containing three fluidic chambers in radial arrangement (see Fig. 3). Multidirectional bending and elongation of the silicone cylinder can be achieved by combining the inflation of the three chambers. Actuating a single chamber leads to bending in one direction, actuating two chambers with the same pressure will generate bending in the plane in between the two chambers, and, finally, inflation of all the chambers together with the same pressure will lead to elongation of the cylinder along its main axis. Intermediate combinations of the three chambers attain the different intermediate module configurations.

The chambers are rounded semicylindrical, and the dimensions are reported in Fig. 3. This shape was chosen in order to increase the available free space in the center (to house the stiffening channel) and on the basis of previous works [35], [36]. In addition in the semicylindrical chamber design, sharp edges were rounded in order to prevent abrupt discontinuities in the material, which could increase the risk of breakage.

The structure was simulated using a finite-element method (FEM). The simulation was performed in Abaqus-Simulia (Dassault Systems) using a dynamic implicit analysis. The mesh used was tetrahedral with quadratic order elements. As expected, the single-chamber inflation determines the bending of the actuator, but with a substantial lateral expansion on the chamber wall, even at low pressures (0.03 MPa). Such behavior was validated experimentally (see Fig. 4, right). The lateral expansion can be tricky especially in a surgical scenario, since it cannot be fully controlled and can generate undesired stress on the surrounding biological structures.

To avoid ballooning, the FFA design has been approached in different ways in the literature, such as by combining stiffer materials and discretizing the overall deformation in smaller cells [37], [38], or by introducing reinforcement fibers [35], [39] or rings [40].

In the proposed design, the balloon containing functionality is obtained using a purpose-built external braided sheath. Braided sheaths are exploited in combination with fluidic actuation in McKibben actuators [41], for developing linear actuators. Such systems are limited in stroke and are not able to achieve large bending angles unless multiple actuators are coupled together as in [42] and [43]. In order to improve multidirectional bending and elongation, we used a crimped braided sheath in the manipulator module. In Fig. 5, the behavior of a standard braided sheath is compared with a crimped sheath in terms of changing its inner diameter (dashed lines on the inset of Fig. 5) with respect to the elongation. The inner diameter is normalized to facilitate the comparison. The curve regarding the standard braided sheath is computed according to [41] starting from the

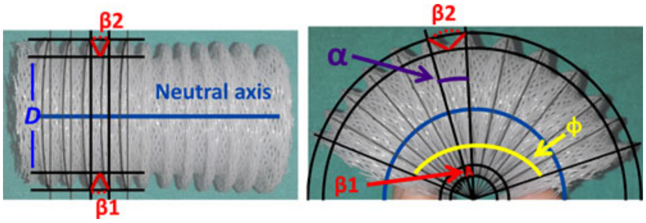

Fig. 6. Analysis of the rearrangements of the crimped structure during bending. *D* is the inner diameter, β_1 and β_2 are the angles between two consecutive bellows, in the outer part of the sheath. The overall bending angle is given by the angle φ and can be seen as the sum of the angles α between the bellows.

measurement of the braiding angle in the maximum and minimum length configurations. This curve follows a third-order polynomial trend; thus, the inner diameter decreases rapidly if the sheath is elongated. The data from the crimped braided sheath were collected experimentally by applying known displacements at one extremity of the sheath and keeping the other one fixed. For each step, the inner diameter was measured. As shown in Fig. 5, the decrease in the inner diameter follows a second-order polynomial trend, thus allowing more than doubled elongations without an excessive shrinkage of the diameter. The crimped braided sheath is also able to undergo large bending angles with a limited decrease in the inner diameter size.

In Fig. 6, the rearrangement in the geometry of the crimped structure is presented. The overall bending of the structure by an angle φ can be considered as the sum of the angles α of which the single crimps are bent among each other. As shown in Fig. 6(right), the inner lumen enclosed inside the bellows in the bent configuration does not vary significantly from the straight configuration shown in Fig. 6(left). This is due to the rearrangement of the fibers that make up the structure at the crimps level (angles $\beta 1$ and $\beta 2$), which changes considerably in the two configurations. Due to its properties, this crimped structure has been recently proposed by King's College London in collaboration with the authors, in the design of a soft endoscope actuated motor driven cables [44].

B. *Design of the Stiffening Mechanism*

The stiffening system needs to comply with the motility of the manipulator module in terms of the elongation and bending capabilities that the module achieves. At the same time, it has to accomplish its main function, which is tuning the robot compliance while interacting with biological structures. This aspect is of utmost importance in flexible medical instrumentation as introduced in [45]. In addition, especially for continuum robots presenting inherently compliant backbones, as in this case, the ability to stiffen part of their body can lead to better compensation for environmental disturbances, thus potentially increasing stability and accuracy [46].

In the proposed design, a granular-jamming-based mechanism is exploited. As stated in [47], jamming entails a phase change in the granular matter due to external stimuli. This variation can be obtained by temperature changes, shear stress, or by an increase in the density of the system (i.e., compacting of the granules). In robotic applications, jamming is typically induced by increasing the density by vacuuming a flexible membrane containing granular matter [48], as shown in Fig. 7(left). Density can be controlled by regulating the vacuum level by making the particles behave like a liquid, a solid, or something in between, thus resulting in a tunable stiffness system. A granular-jamming-based stiffening mechanism was selected because it conforms to highly deformable structures. Its shape, in the nonjammed configuration, is mainly due to the properties of the containing membrane [49]. Additional advantages consist of fast activation, easy fabrication, and typically limited production costs. Because of its unique features, many groups have integrated granular jamming into soft robotic devices without rigid parts or backbone-like structures [50]–[53]. It has been successfully integrated in elastomeric structures in combination with fluidic actuation in [51] where granular jamming was used to change the stiffness of selected areas on a sphere in order to change its response to internal inflation and in [54] where pneumatic actuation was exploited to enhance the stiffness variation of a granular jamming system for the remote palpation of organs. Combining FFA and a granular-jamming-based stiffening system preserves the flexibility of the structure and enables the stiffness to be increased to carry out specific tasks. For example, it is possible to provide higher stability and disturbance rejection or increased efficiency during the application of forces to a target.

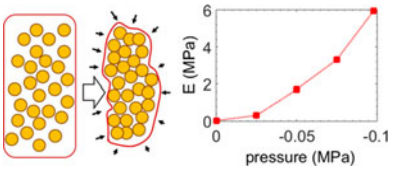

Fig. 7. (Left) Scheme of the granular jamming phenomenon. (Right) Change in the Young modulus at different vacuum levels of the stiffening chamber computed from stress–strain curves after tensile tests.

For the first implementation of the stiffening system, a solution based on a latex membrane was selected with coffee powder as granular material, in line with previous research [50], [52].

The change in the elastic modulus of the stiffening chamber under different pressure levels was measured by performing stress–strain tests with an Instron testing machine. Fig. 7(right) shows the changes in the elastic modulus (E) at three different pressures[1]: atmospheric pressure (0 MPa), −0.049 MPa, and −0.098 MPa. The elastic modulus at atmospheric pressure is 0.27 MPa, which is lower than the pressure/stiffness of the silicone in the actuator, thus not altering its flexibility. On the other hand, the stiffness reaches 1.7 MPa at −0.098 MPa pressure (5.3 times higher) and 5.9 MPa at full vacuum −0.098 MPa).

The stiffening chamber is housed in an 8-mm channel in the center of the actuator of Fig. 3. The shape and dimension of the stiffening chamber were simplified for this study in order to have a fully integrated system and evaluate its overall performance as a proof of concept. More complex shapes maximizing the volume of granules may increase the stiffening range. Indeed, previous works done by King's College London in

---

[1] All pressures along the manuscript are related to the atmospheric pressure.

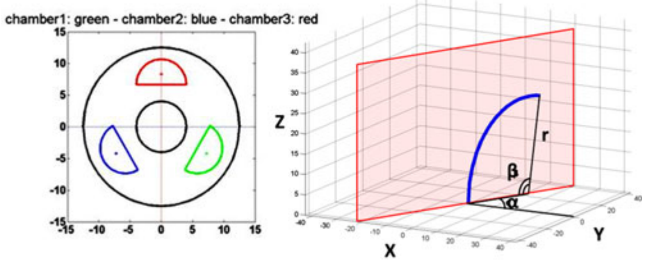

Fig. 8. (Left) Illustration of model geometry. (Right) Scheme of the parameters defining the position and orientation of the module, according to the constant curvature model.

collaboration with the authors demonstrated that the containing membrane plays an essential role in the performance of the system [49].

The final dimensions and design of the module integrating all the aforementioned functionalities are reported in Section IV-C.

C. Analytical Modeling

In order to model the structure motion capabilities, an analytic model was developed. The model is based on the constant curvature assumption, as in [55], and on the flexible actuator model described in [56].

The flexible actuator model described in [56] is considered accurate for small deformations. We used the same basic equations (reported in this section) except for various experimental correcting factors, which were introduced in order to compensate for this limitation. The effect of external forces is not considered in the model.

Fig. 8 reports the geometry of the model.

Considering the three chambers with internal pressures $P_i (i = 1, 2, 3)$, from the equivalents of the bending moment vectors on the *xy* plane, we have

$$\tan \alpha = \left(\frac{\sqrt{3}\,(2P_1 - P_2 - P_3)}{3\,(P_2 - P_3)} \right) \qquad (1)$$

where P_i represents the pressure of the *i*th chamber and α_i, the *i*th chamber bending angle (angle between the bending plane and the center—*i*th centroid segment). From (1), it is possible to derive the bending direction angle, which also defines the rotation axis of the cross section (in blue in Fig. 8, right). Once the bending plane is completely defined, the curvature radius (*r*) can be calculated by using material data on Young's modulus and the area moment of inertia, as

$$r = \frac{3EI}{A_p d \sum_{i=1}^{3} (P_i \sin \alpha_i)} \qquad (2)$$

where A_p is the total pressurized area of the cross section, and *d* is the distance between the central axis of the module and the chamber centroids. *E* and *I* are the Young's modulus of the material and the moment of inertia of the module, respectively.

The final length of the manipulator (*L*) can be evaluated as

$$L = \frac{A_P L_0}{3A_0 E} \sum_{i=1}^{3} P_i + L_0. \qquad (3)$$

where A_0 is the total base area of the cross section, and L_0 is the rest length of the module.

Given the constant curvature assumption, the bending angle is evaluated through the ratio between the final length of the module and the curvature radius calculated above

$$\beta = \frac{L}{r}. \qquad (4)$$

The necessary calculations, which take into consideration the arrangement and shape of the chambers, were applied to the equations above to mimic the specific case of the single-module manipulator.

All the parameters necessary for the implementation of the above equations are geometrical entities and can be arbitrarily defined or left as a variable for optimization purposes. The only physical parameter is represented by the Young's modulus of the module. Taking into account all the assumptions at the base of the model, it is clear that this kind of tool cannot be considered a precise way to predict the module behavior, but it is very useful for a general understanding of its combined functionalities and provides faster results compared to an FEM-based approach.

A more extensive FEM modeling of the entire structure can lead to modeling of components presenting highly nonlinear behavior and with complex interactions with each other. However, this modeling approach is not addressed in the paper. More accurate models of the manipulator can be found in [57] and [58]. In [57], a strategy for performing accurate position control of the single module is presented. After the characterization of the single components of the module, the output of the model was compared with the actual performance of the module.

For a more comprehensive understanding of the module behavior, extensive experimental characterizations were carried out on the fully integrated module, as presented in Section V.

IV. MODULE FABRICATION

In this section, the fabrication of all the components of the complete module and their assembly is described.

A. Fabrication of the Crimped Braided Sheath

The crimped braided sheath is created starting from an off-the-shelf flexible braided sheath (RS Components) with a maximum reachable inner diameter when fully compressed of 33 mm [see Fig. 9(a)]. A 25-mm-diameter cylinder is then put inside the sheath, which is manually compressed until it starts to form the bellows [see Fig. 9(b)]. The sheath is then kept in place and heated with a heating gun to obtain a permanent deformation. The temperature depends on the material of the sheath. With the current one made of polyester, a temperature of 350 °C was used for approximately 15 min. At the end of the process, the crimped braid is obtained as in Fig. 9(c).

B. Fabrication of the Stiffening Chamber

The stiffening chamber is composed of an external latex membrane (condom from TheyFit, http://www.theyfit.co.uk/size J33) 21.6 mm in diameter and 88 mm in length. The top and bottom parts of the membrane are cut; the top part is closed by tying a

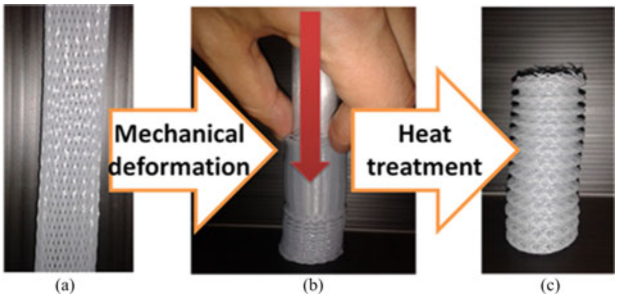

Fig. 9. Fabrication phases of the crimped braided sheath. The commercial sheath (a) is pushed and forced to slide on a cylinder to produce crimps (b), and after the heating process, the crimped structure remains stable (c).

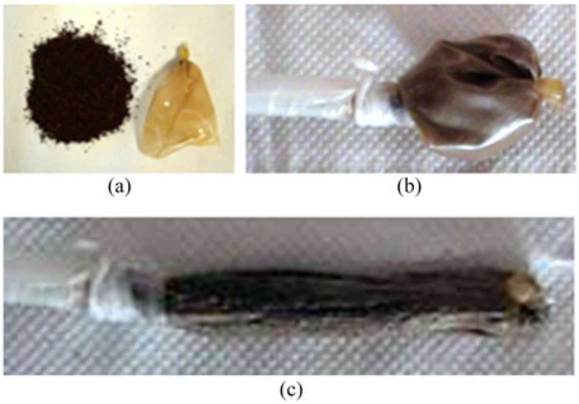

Fig. 10. Fabrication phases of the stiffening chamber. The flexible membrane and the granular material (a) are assembled to form the stiffening chamber (b), which is vacuumed and shaped for its introduction into the stiffening channel (c).

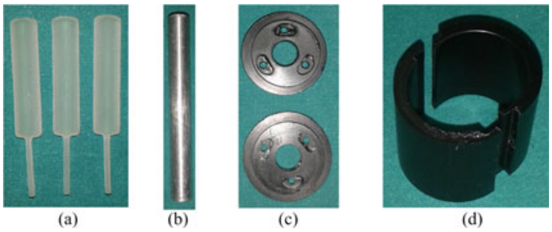

Fig. 11. Components of the mold used for the fabrication of the silicone structure of the module. (a) and (b) Molds for the fluidic chambers and for the stiffening chamber, respectively. (c) Two caps of the mold. (d) Two shells closing the mold.

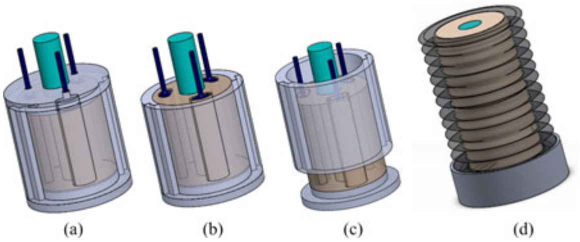

Fig. 12. Fabrication steps of the silicone structure of the module. (a) Pouring of silicone in the fully assembles mold. (b) Opening of the mold after curing. (c) Moving up of the outer shells for additional pouring of silicone on top. (d) Fixing of the external crimped sheath to the actuator.

knot with a soft wire and using silicone glue [see Fig. 10(a)]. The membrane is filled with 5 g of coffee, a 2 mm pipe is inserted, and the membrane is sealed around it with Parafilm [see Fig. 10(b)].

C. Fabrication of the Complete Module

The FFA is fabricated by pouring silicone into a mold. The mold is composed of different components as shown in Fig. 11. The negative parts corresponding to the fluidic chambers are fabricated using a 3-D Printer Invision Si2, Inition, with VisiJet XT 200 as an acrylic photopolymer, and VisiJet S100 as support material [see Fig. 11(a)]. The fluidic chamber mold comprises 2-mm channels used for housing the pipes for the air supply. In the design of the chambers, all the sharp edges are rounded in order to avoid abrupt discontinuities, which can increase the risk of breakage during air inflation. The chambers are aligned by exploiting dedicated cuts on the two bases [see Fig. 11(c)]. These are fabricated starting from 3-mm-thick Delrin sheets using a laser cut machine (VLS 3.50). An 8-mm-diameter aluminum bar [see Fig. 11(b)] is used as a central channel mold. Two half cylindrical Delrin shells are used to close the mold [see Fig. 11(d)].

The fabrication of the complete module is performed through several steps. First, the silicone is poured into the fully assembled mold, as shown inFig. 12(a). Thus, the grooves on the two plates of the mold [see Fig. 11(c)] guarantee the correct alignment of the chambers. Once the silicone is polymerized, the upper base is removed [see Fig. 12(b)] and the semicylindrical shells are moved up 10 mm [see Fig. 12(c)]. Silicone is poured again in order to close the fluidic chambers. When the casting of the silicone is complete, the same procedure is repeated on the opposite side. With this process, the fluidic actuators are obtained as shown in Fig. 3, but with a central hole for housing the stiffening chamber. The external sheath is then slid around the fluidic actuators and is fixed only at its extremities when it is at maximum compression, in order to maximize its elongation capabilities. The actuator with the braided sheath around is put in a 30-mm inner diameter and 5-mm height cylinder. Silicone is then poured between the outer cylinder and the external part of the fluidic actuators to seal the braided sheath to the actuator, as shown in Fig. 12(d). The same procedure is executed on the opposite side. Thus, the sheath is fixed to the actuator only at the top and bottom, while in relation to the fluidic chambers, it is still able to slide freely. Finally, the fluidic chamber mold and the central chamber mold are removed through the 2-mm channels left for the pipes, by exploiting the high deformability of the silicone. In these channels of 2 mm as outer diameter, 1.2-mm inner diameter polyurethane tubes (SMC Corporation) are introduced and sealed with Sil-Poxy silicone rubber adhesive (Smooth on Inc.) for the air supply.

The granular-jamming-based stiffening chamber is integrated in the central channel after having vacuumed and shaped it for it to be fitted inside the module's inner channel [see Fig. 10(c)]. The vacuum is then released to enable the stiffening chamber to conform to the silicone channel of the FFA. The chamber is then fixed at the extremities, using Sil-Poxy silicone rubber

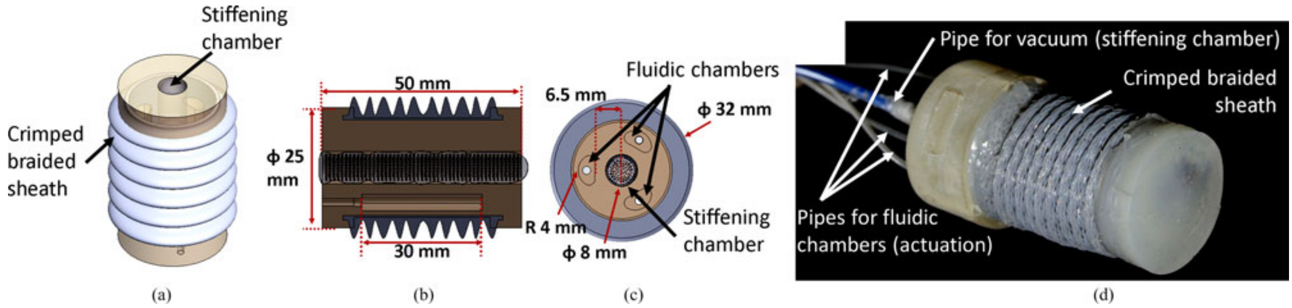

Fig. 13. STIFF-FLOP module with its final dimensions. (a) Isometric view. (b) Lateral section view. (c) Top section view. (d) Fabricated prototype.

adhesive (Smooth on Inc.). Additional silicone is poured on the top and bottom of the manipulator in order to fully enclose the stiffening system.

The complete module with the final dimensions is shown in Fig. 13(a) and (b), while the complete fabricated prototype is reported in Fig. 13(c).

For a multimodule manipulator, different modules are connected by pouring silicone between them in order to have a continuum in the mechanical properties. Stiffening and actuation of the different segments are kept independent for a number of modules not higher than three. Two main approaches can be used to pass through the pipes necessary for actuation and stiffening of the distal modules: 1) multipiping and 2) onboard valves. The success of the first strategy strictly depends on the ability of the pipes to follow the movements of the manipulator and still be functional. For this reason, the two alternatives under evaluation are: 1) to leave the pipes on the external surface and 2) to use flexible silicone pipes (i.d. 0.8 mm, e.d. 1.5 mm, Cole-Parmer) that can be passed through the fluidic and stiffening chamber with some extra length available, as illustrated in Fig. 14. The multipiping approach is mainly exploited to evaluate the performance of a multimodule manipulator. This is because it can be affected by leaking issues, and the encumbrance introduced by the pipes limits the number of modules that can be interconnected. A study on a simplified two-module structure is presented in [27]. The study focuses on how a manipulator composed of two identical modules that can be independently actuated and stiffened and can be used for medical tasks such as retraction of multiple organs. In addition, it shows how stiffness variation can be exploited for increasing efficiency during the application of forces on different targets.

The second approach (integrated valves) consists of two main lines along the manipulator: a pneumatic and a vacuum line. The interconnection between the modules is still based on silicone, but integrating a microvalve for each chamber of each module that regulates the vacuum or air pressure [59]. Although this strategy is promising, it introduces several technical challenges in the development and integration of the valves, which is well beyond the aims of this work. The development of a multimodule manipulator will be addressed in future works.

V. EXPERIMENTAL CHARACTERIZATION OF THE SINGLE MODULE

The active motion of the module was performed by controlling the pressure in each fluidic chamber independently. Three proportional pressure regulator valves (series K8P, E.V.P. systems) modulate the air pressure inflated in each chamber. A compressor (Compact 106, Fiac Air-Compressors) was used as a pneumatic air source. A vacuum for stiffness modulation was obtained by using a vacuum pump (LB.4, D.V.P. vacuum technology), which provides a maximum vacuum of 0.03-Pa absolute pressure with a flow of 3 m^3/h. The vacuum generated inside the stiffening chamber was monitored with a pressure sensor (SWCN-V01-P3-2, Camozzi) and resulted in a maximum of -0.0987 MPa relative pressure. A 5-μm filter (MC104-D10, E.V.P. systems) was used to prevent particles from entering the pump. A vacuum reducer with pneumatic regulation (110130, E.V.P. systems) was used in combination with a pressure regulator valve (series K8P, E.V.P. systems) powered by the compressor in order to control the vacuum level in the stiffening chamber.

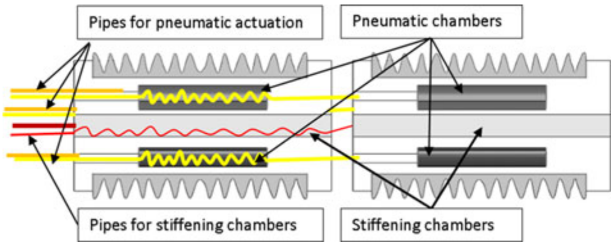

Fig. 14. Example of connection of two modules by using flexible silicon pipes passed through the fluidic and stiffening chambers. In light red and light yellow, the pipes coming from the distal module are drawn; in dark yellow and dark red, the pipes coming from the proximal module.

All the pressure regulators are controlled with low-pass filtered pulse width modulation (PWM) signals generated from the digital I/O pins of the RoNex MkII (http://www.shadowrobot.com/products/ronex/). The pressure within each chamber can be regulated by setting the period and the ON-time of the PWM signal for every pin. The RoNex MkII is programmed using robot operating system (ROS).

A. *Workspace Analysis*

The workspace of the single-module manipulator was obtained by placing a six-degree-of-freedom (DOF) probe (Northern Digital Inc.) on the tip of the module as shown inFig. 15. The pressure range tested in the chambers was from 0 to 0.065 MPa.

Since the module motion in response to the applied pressure is not linear, the following pressures were tested: [0.000 0.025 0.035 0.045 0.050 0.065] MPa. These pressures were found to

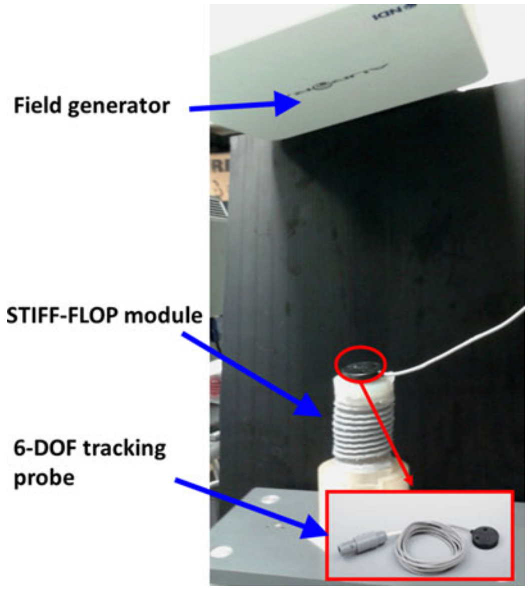

Fig. 15. Setup for the experimental measurement of the workspace of the STIFF-FLOP module. The 6-DOF localization probe is highlighted in red.

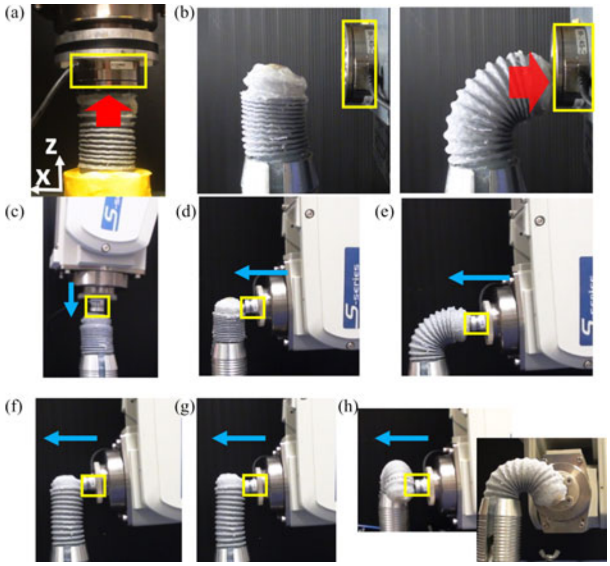

Fig. 16. Force and stiffness characterization setups; the F/T sensor position in the different tests is highlighted with a square. (a) Setup for measuring the force generated by the module in isometric condition; the arrow indicated the direction toward the module is applying force. (b) Setup for evaluating the force applied on a laterally places target: on the left the initial position of the module with no chamber inflation; on the right the module in applying a force to the F/T sensor with a 0.065 MPa pressure in one chamber. Different testing conditions for evaluating the stiffness variation of the module. (c) Base condition axial displacement. (d) Base condition imposing a lateral displacement. (e) 90° bending axial displacement. (f) and (g) Lateral displacement at different elongation conditions. h) Lateral displacement during single-chamber bending. The blue arrows indicate direction of the imposed displacement.

significantly describe the motion of the module in a previous work [28].

In order to derive the full manipulator workspace, all the different combinations of the aforementioned pressures were applied in the three chambers, thus obtaining 6^3 combinations (i.e., 216 points). Each pressure combination was automatically set by the control system in ROS. Between two pressure combinations, the manipulator was reset to the base position by imposing 0-MPa differential pressure in all the chambers. During the application of each combination of pressures, the position and orientation of the module tip was acquired with the Aurora EM Tracking system for 1 s (i.e., 100 samples).

B. *Model Validation*

The analytical model of Section III-C was compared with the experimental results obtained from the characterization tests of a single module. The model outputs were compared with the results of the experimental tip tracking of one module (same setup as for the workspace analysis, Fig. 15). The aim of the experimental tests was to measure the position of the module tip at increasing pressures of a single chamber. The tip position is considered in terms of length and bending angle of the module, which are sufficient parameters to completely describe the configuration of the module (given the constant curvature assumption).

C. *Force Characterization*

The module force was measured by positioning an F/T sensor (MINI 45, ATI, USA, resolution = 0.025 N), connected to a fixed structure [see Fig. 16(a)] and placed in contact with the module tip. This way, the length of the module was constrained. The force generated from one chamber, two chambers, and three chambers was measured using pressures ranging from 0.00 to 0.08 MPa. In this case, the tested pressures were higher than the workspace evaluation test in order to evaluate the maximum force (in isometric conditions) that could be generated by the module without damaging it.

A comprehensive assessment of the ability to apply forces by the module can be very challenging due to the softness of the device. In fact, the force performances are expected to differ depending on the different configurations of the module due to the change in the tensional state of the system. Thus, an additional test to evaluate the possibility of applying forces laterally when bended was performed. The test consisted in positioning the module in the vertical position and fixing its base. The F/T sensor was then positioned laterally, as shown Fig. 16(b), in order to measure the forces applied at different inflation pressures in one chamber, with the module bending. The range of pressures tested started from the minimum pressure value needed to start being in contact with the F/T sensor, which was 0.04 MPa.

D. *Stiffness Characterization*

The stiffening performance of the complete module was experimentally characterized by imposing controlled displacements at the tip of the module through a 6-DOF industrial robot (RV-6SL, Mitsubishi) with an F/T sensor (NANO17, ATI, USA, resolution = 0.00625 N) fixed on its end effector. This way, it was possible to impose the desired orientation of the load cell with respect to the module tip position, while varying the configurations of the module and tuning the stiffening.

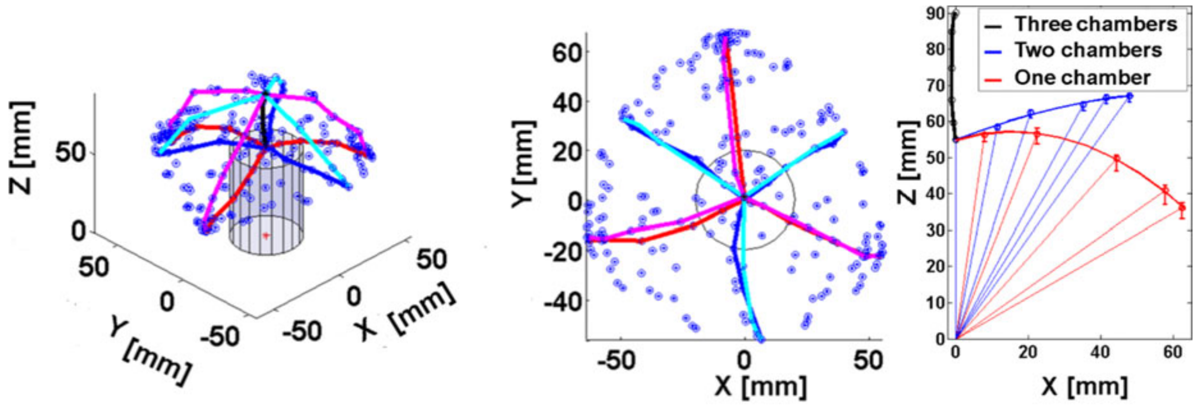

(a) (b) (c)

Fig. 17. Experimentally evaluated workspace of the STIFF-FLOP module. (a) Isometric view, (b) top view, and (c) trajectories of the tip during single-chamber bending, two-chamber bending, and elongation.

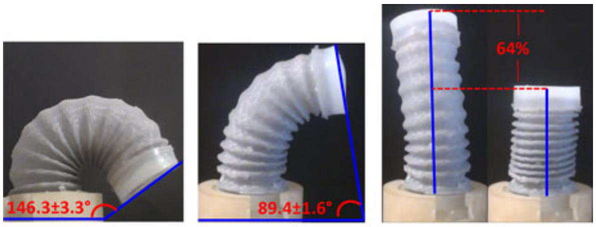

(a) (b) (c)

Fig. 18. Fabricated STIFF-FLOP module performing bending with a (a) single-chamber inflation and (b) two-chamber inflation; in (c), elongation due to the inflation of all the three chambers at the same time is demonstrated.

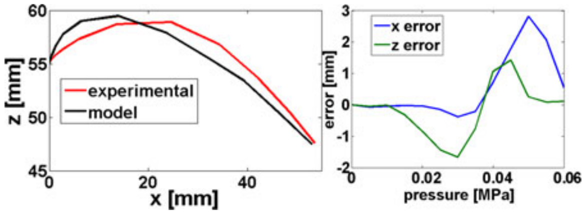

Fig. 19. Quantification of the model error in describing the module behavior during bending: direct comparison of the tip trajectory (left) and error plot of both x and z components (right).

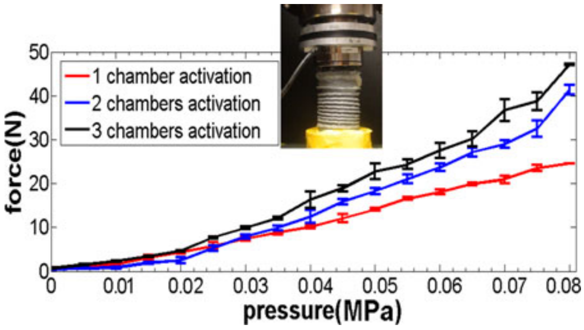

Fig. 20. Force measured by actuating one, two, and three fluidic chambers of the STIFF-FLOP module in isometric conditions.

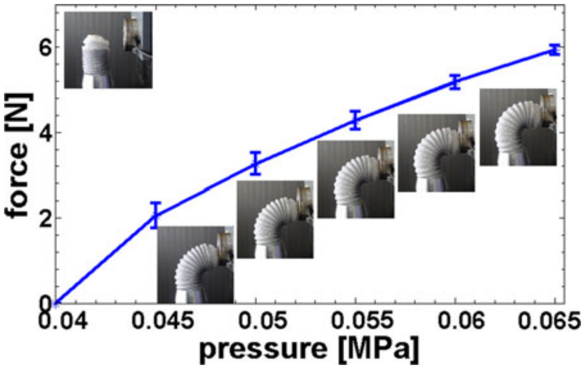

Fig. 21. Force applied on a laterally placed load cell by the STIFF-FLOP module at different pressures. In the insets, the corresponding images on the module are reported to visualize the change in curvature.

The stiffness variation was characterized in four different conditions: 1) base condition [no actuation of the fluidic chambers, lateral displacement; see Fig. 16(c)]; 2) base condition [axial displacement; see Fig. 16(d)]; 3) 90° bending condition by inflating a single chamber with a pressure of 0.04 MPa, displacement along the axis of the module [see Fig. 16(e)]; and 4) two different elongation percentages by inflating all three fluidic chambers with a pressure of 0.035 [see Fig. 16(f)] and 0.045 [see Fig. 16(g)], lateral displacement. In conditions 1) and 4), the imposed displacement was 10 mm (lateral displacement). In cases 2) and 3), where the module was tested in the axial direction, a displacement of 5 mm was imposed.

An additional test was performed to evaluate the stiffening performance in different configurations of the manipulator by imposing a 10-mm lateral displacement during different single-chamber bending conditions starting from the base condition to the maximum bending angle [see Fig. 16(h)].

All the aforementioned tests were carried out both without activating the stiffening chamber (atmospheric pressure, 0.0 MPa) and at the maximum obtainable vacuum level with the setup used (–0.098-MPa relative pressure in the stiffening chamber). Each test was repeated three times.

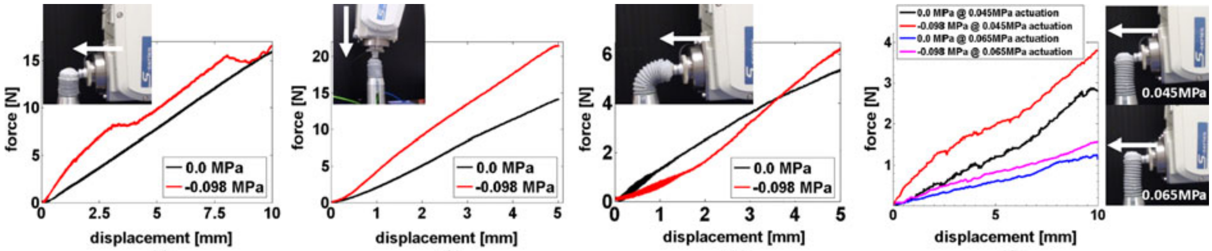

(a) (b) (c) (d)

Fig. 22. Force–deformation curves obtained during the stiffness characterization of the STIFF-FLOP module. In the inset, the experimental setup is shown and the direction of the imposed displacement is highlighted by the white arrow. In the plot, the red and magenta curves correspond to the case of fully vacuumed stiffening chambers, while the black and blue curves correspond to the case when the module was not stiffened. (a) Lateral displacement with no chamber inflation. (b) Axial displacement with no chamber inflation. (c) Axial displacement, single-chamber inflation of 0.04 MPa. (d) Lateral displacement, three-chamber inflation at two different pressures: 0.045 MPa (red and black curves) and 0.065 MPa (magenta and blue curves).

VI. RESULTS AND DISCUSSION

A. Workspace Analysis

As mentioned in this section, for each of the 216 pressure combinations in the three fluidic chambers, the position of the module tip was acquired for 1 s, corresponding to 100 samples. Fig. 17(a) and (b) reports the average of the 100 samples for each tip position.

Fig. 17(a) reports the isometric view of the point cloud. A cylinder with real module dimensions was added at the axes origin. The red lines in Fig. 17 correspond to the tip position during single-chamber activations, while the blue lines correspond to activation of the two chambers (same pressure in both at each time). The black line is the trajectory of the tip when all the three chambers were inflated at the same pressure (elongation).

In order to provide a more intuitive representation of the workspace, the points creating the upper shell and corresponding to the single- and double-chamber activation are highlighted in cyan and magenta, respectively.

Fig. 17(b) shows the top view of the workspace. The shape is almost circular, as theoretically expected, and in correspondence to the single-chamber activation lines, it extends slightly more outward. As highlighted by Fig. 17(b), the system presented good symmetry properties (with 120° phase) in its behavior, thus proving that during fabrication, no substantial defects were introduced.

Fig. 17(c) reports trajectories of the tip of the module during the single- and double-chamber bending and the elongation at the different pressures tested. The plotted data of the trajectories during bending [see Fig. 17(c)] are obtained by realigning the curves in the three directions with a rotation along the z-axis of 120° and calculating the average curves. Both the single-chamber and the two-chamber bending trajectory were fitted with a second-order polynomial. As a result of the fitting, the single-chamber bending trajectory presented an R^2 of 0.998 with a root-mean-square error (RMSE) of 0.4, while the two-chamber bending trajectory, again fitted with a second-order polynomial, resulted in a R^2 of 0.99 with an RMSE of 0.56.

The maximum bending angle both in the case of single- and two-chamber activations was found from the measured tip orientation data. In the case of the single-chamber bending, the average maximum bending angle was 146.3° ± 3.3° and in the case of two-chamber bending, it was 89.4° ± 1.6°. The maximum elongation achieved by increasing the pressures in the three chambers at the same time was 64%, thus reaching a final length of 82 mm. To summarize, Fig. 18 shows the module with the aforementioned performances. The video shows the module performing single- and two-chamber bending as well as elongation.

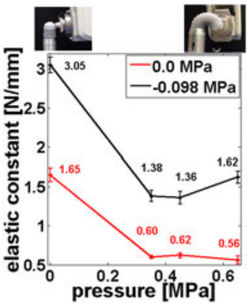

Fig. 23. Change in the elastic constant of the STIFF-FLOP manipulator, at different inflation pressures in a single fluidic chamber: comparison between the stiffened configuration (red curve) and the floppy one (black curve). The numerical values of the elastic constant are reported on the plot.

B. Model Validation

The model described in Section III-C was compared with experimental results obtained from the workspace analysis of a single module. To facilitate the comparison, the two tip trajectories were plotted together in Fig. 19(left), where the error is clearly shown. In Fig. 19(right), the error is quantified along the x- and z-axes. The model does not perfectly fit the experimental results, and the maximum calculated error (normalized to the length of the module) corresponds to 4%. Despite this, the model follows the highly nonlinear behavior of the module.

C. Force Characterization

Results from the force measurements in isometric conditions are reported in Fig. 20. One single chamber is able to generate 24.6 N increasing almost linearly in relation to the input pressure. By activating two and three chambers, the force reaches 41.4 and 47.1 N, respectively.

TABLE I
RESULTS FROM STIFFNESS CHARACTERIZATION

Test type		Elastic constant (N/mm) with no stiffening	Elastic constant (N/mm) with active stiffening[1]	Elastic constant increase (%)
Axial tests	No chamber inflation	3.05 ± 0.11	5.36 ± 0.09	75.70
	90° bending (0.04 MPa pressure in one chamber)	1.23 ± 0.10	1.63 ± 0.11	32.52
Lateral tests	Elongation (0.045 MPa pressure in the three chambers)	0.31 ± 0.02	0.53 ± 0.03	73.14
	Elongation (0.065 MPa pressure in the three chambers)	0.11 ± 0.01	0.16 ± 0.01	44.66

[1] internal pressure set to −0.098 MPa.

Fig. 21 shows the results from the lateral force measurements, with one chamber activated. Since the module reaches 90° bending at approximately 0.04 MPa, lower pressures are not reported. The maximum force measure at 0.065 MPa was 5.95 ± 0.11 N.

D. *Stiffness Characterization*

Tests were performed in different configurations of the module, in order to evaluate the effectiveness of the stiffening system. An example of stiffness testing experiment is shown in the video.

The plots in Fig. 22 show that the force required to deflect, in the case of lateral tests, or to compress, in the case of axial tests, increases significantly when the stiffening system is activated (−0.098 MPa pressure). As expected, during lateral testing, abrupt changes in the stiffness may occur due to the granular nature of the material in the stiffening chamber. Indeed, if the applied force is substantial, the granules that are kept together by the vacuum pressure can start to separate, thus decreasing the stiffness. This is clearly observed in Fig. 22(a), for the lateral test with no chamber inflation. Indeed, when the stiffness is activated, two plateaus can be found. After the second plateau, the stiffening system is no longer effective, and the behavior of the module is in line with the case of no activated stiffening. The Young's modulus of the device was estimated from the lateral test in the nonactuated condition by considering the module as a deflected beam. When the stiffening chamber is not activated (not vacuumed), the Young's modulus is 1.6 ± 0.1 MPa and reaches 3.64 ± 0.08 MPa when stiffened (vacuumed). In the other configurations, the elastic constant was calculated and used as indication of the stiffness variation. The elastic constant is computed as the slope of the first linear tract in the force–displacement results from the stiffening tests. As expected, when no actuation is provided, the stiffness variation is important both for the axial and lateral directions (75.7% and 85.55%, respectively).

Two different elongation levels were tested, 45% (0.045 MPa) and 65% (0.065 MPa), as shown in Fig. 22(d). With respect to the nonactuated condition, the stiffness increasing trend diminishes as expected, since the internal structures are stretched and thus reduced in section. Although the overall stiffness in the module decreases considerably when elongated or bent, the stiffness variation is still evident.

In the specific configuration of the 90° bending axial test [see Fig. 22(c)], we observed that for the first 2.5 mm, the stiffness when vacuum is applied starts to follow a linear trend and is lower than the nonstiffened case. The reason for this is that the granules are separated due to the bending. Indeed, during bending, the change in length of the side of the manipulator is significant (it approximately doubles). Thus, when the tip of the module is pressed, the granules start compressing. This happens for the first 2 mm, after which the effectiveness of the stiffness chamber is restored. The change in the elastic modulus in this specific case for the stiffened condition is measured in the range 2–3.5 mm. Once the granules have recompacted, the stiffness increases linearly and exceeds the case when no vacuum is applied.

Stiffening performances during single-chamber bending of the module are reported in Fig. 23 where the variation in the elastic constant at different pressures in one chamber is plotted. Each point in Fig. 23 was computed as the slope of the first linear tract in the force–displacement results at different single-chamber inflation pressures. The direction of the displacement was lateral as shown in the inset of Fig. 23; the numerical values are reported in the last four rows of Table I. Note that the stiffness increase is preserved at the different inflation pressures. At the maximum pressure tested, the stiffness tends to increase slightly, probably because the internal structures are already highly pressurized due to the inflation of all the three chambers.

Table I reports the numerical results for all the stiffness characterization, along with their variability. The elastic constants computed during each test are reported both when the stiffening system is activated and when it is not, and the percentage increase in the stiffness of the module is indicated.

Shape modifications of the stiffening chamber during the module motions may alter the mechanical properties of the stiffening chamber itself. However, although with a different efficiency, the stiffening mechanism still provides an important change in stiffness properties of the module.

VII. CONCLUSION

This paper has presented the concept and design of a new modular manipulator for MIS. The fabrication of its components has been detailed, and extensive characterizations of its performances have been provided. Some insights on the integration strategy of multiple module have been also provided. An analytical model was introduced and validated through experimental tests.

Due to the complex interactions among the structures of the module (crimped sheath, highly deformable silicone, and granular-jamming-based stiffening mechanism), an experimental approach was selected in order to evaluate the system performances. However, an analytic model was presented and validated. This model was exploited in the design phase of the single module. Future research is required to develop a reliable model taking into account all the different interactions among the components of the module in order to accurately control the robot.

In parallel to more accurate modeling, integration of sensors will play an essential role in the control of the shape of the manipulator, as well as for its interactions with the surgical environment. In order to preserve the MRI compatibility of the robot, techniques based on light intensity modulation seem to be good candidate technologies. Sensors for shape monitoring of the module were proposed in [60], while in [61] and [62], force and tactile sensing were proposed. Future work will address the integration of sensing elements in the module.

The proposed device is capable of applying high forces, which could be useful for the surgical scenarios introduced in Section II. Typical retraction tasks [10] require forces between 0.9 and 3.3 N for NOTES procedures [14] or higher, with more standard procedures where lifting an organ such as the liver (normally weighs about 1.5 kg) is required. This makes the module a good candidate for retraction. The accuracy and repeatability do not currently fully satisfy the requirements for accurate manipulation and indicate that the most suitable application of the current version of the manipulator is a surgical retractor. Further developments in the modeling and control of the actuator are needed for increasing performances in this direction. Despite the softness of the material used that intrinsically guarantees a safer interaction between the module and the tissues, extensive *ex vivo* and *in vivo* tests are needed for a concrete validation, although initial studies demonstrate globally safe interaction *in vivo* [63].

A granular-jamming-based stiffening mechanism was introduced to modulate the module's overall stiffness and was accurately characterized, particularly focusing on its integration onboard the single module. Although the stiffness range is not optimal and can be improved through future design optimizations, which could involve noncircular shapes in the center, this system was able to provide stiffness variations in different configurations of the module. At the same time, it followed the high deformability of the structure, without compromising its dexterity. This demonstrates the high potential of combining flexible fluidic actuation with granular-jamming-based stiffening mechanisms.

The module demonstrated high dexterity in terms of bending and elongation. In addition, thanks to the lack of a fixed backbone, it has a highly compressible structure, which allows it to be squeezed through access ports smaller than its nominal diameter, without causing damage to the manipulator's functionalities. In a multiple module scenario, as devised in Section IV-C, the hyperredundancy in the structure could enable multiple tasks to be performed with the same arm, as well as multiple controlled interactions with the biological structures along the manipulator, thus paving the way for a completely new approach in performing surgical procedures.

ACKNOWLEDGMENT

The authors would like to thank the STIFF-FLOP Consortium for their useful suggestions and discussions related to the design of the surgical module.

REFERENCES

[1] V. Vitiello, S. Lee, T. Cundy, and G. Yang, "Emerging robotic platforms for minimally invasive surgery," *IEEE Rev Biomed Eng.*, vol. 6, pp. 111–126, 2013.

[2] (2015, Oct.). [Online]. Available: http://www.intuitivesurgical.com/

[3] A. Degani, H. Choset, A. Wolf, and M. A. Zenati, "Highly articulated robotic probe for minimally invasive surgery," in *Proc. IEEE Int. Conf. Robot. Autom.*, May 2006, pp. 4167–4172.

[4] W. Wei, X. Kai, and N. Simaan, "A compact two-armed slave manipulator for minimally invasive surgery of the throat," in *Proc. IEEE/RAS-EMBS Int. Conf. Biomed. Robot. Biomechatron.*, Feb. 2006, pp. 769–774.

[5] A. Bajo, L. M. Dharamsi, J. L. Netterville, C. G. Garrett, and N. Simaan, "Robotic-assisted micro-surgery of the throat: The trans-nasal approach," in *Proc. IEEE Int. Conf. Robot. Autom.*, May 2013, pp. 232–238.

[6] J. Burgner, P. J. Swaney, R. A. Lathrop, K. D. Weaver, and R. J. Webster, "Debulking from within: A robotic steerable cannula for intracerebral hemorrhage evacuation," *IEEE Trans. Biomed. Eng.*, vol. 60, no. 9, pp. 2567–2575, Sep. 2013.

[7] A. Bajo, R. E. Goldman, W. Long, D. Fowler, and N. Simaan, "Integration and preliminary evaluation of an insertable robotic effectors platform for single port access surgery," in *Proc. IEEE Int. Conf. Robot. Autom.*, May 2012, pp. 3381–3387.

[8] J. Shang, D. P. Noonan, C. Payne, J. Clark, M. H. Sodergren, A. Darzi, and G. Z. Yang, "An articulated universal joint based flexible access robot for minimally invasive surgery," in *Proc. IEEE Int. Conf. Robot. Autom.*, May 2011, pp. 1147–1152.

[9] N. Y. Mehta, R. S. Haluck, M. I. Frecker, and A. J. Snyder, "Sequence and task analysis of instrument use in common laparoscopic procedures," *Surgical Endoscopy Other Interventional Tech.*, vol. 16, no. 2, pp. 280–285, 2001.

[10] M. Hashmonai and D. Kopelman, "Sling retraction of the falciform ligament to ameliorate exposure in laparoscopic upper abdominal surgery," *Surgical Laparoscopy Endoscopy*, vol. 6, no. 1, pp. 71–72, 1996.

[11] D. C. Steinemann, P. Limani, P. A. Clavien, and S. Breitenstein, "Internal retraction in single-port laparoscopic cholecystectomy: Initial experience and learning curve," *Minimally Invasive Therapy Allied Technol.*, vol. 22, no. 3, pp. 171–176, 2013.

[12] S. Park, R. A. Bergs, R. Eberhart, L. Baker, R. Fernandez, and J. A. Cadeddu, "Trocar-less Instrumentation for laparoscopy magnetic positioning of intra-abdominal camera and retractor," *Ann. Surgery*, vol. 245, no. 3, pp. 379–384, 2007.

[13] G. Tortora, M. Salerno, T. Ranzani, S. Tognarelli, P. Dario, and A. Menciassi, "A modular magnetic platform for natural orifice transluminal endoscopic surgery," in *Proc. 35th Annu. Int. Conf. IEEE. Eng. Med. Biol. Soc.*, Jul. 2013, pp. 6265–6268.

[14] G. Tortora, T. Ranzani, I. De Falco, P. Dario, and A. Menciassi, "A miniature robot for retraction tasks under vision assistance in minimally invasive surgery," *Robotics*, vol. 3, no. 1, pp. 70–82, 2014.

[15] M. Ryou and C. Thompson, "Magnetic retraction in natural orifice transluminal endoscopic surgery (NOTES): Addressing the problem of traction and countertraction," *Endoscopy*, vol. 41, pp. 143–148, 2009.

[16] Safe Retraction based on magnetic forces and polymeric films—-SACTIONPOL, Intuitive Surgical Grant Program 2013.

[17] D. Trivedi, C. Rahn, W. Kier, and I. Walker, "Soft robotics: Biological inspiration, state of the art, and future research," *Appl. Bionics Biomech.*, vol. 5, pp. 99–117, 2008.

[18] I. D. Walker, "Continuous backbone "continuum" robot manipulators," *ISRN Robotics*, vol. 2013, art. ID 726506, 2013.

[19] M. Cianchetti, T. Ranzani, G. Gerboni, T. Nanayakkara, K. Althoefer, P. Dasgupta, and A. Menciassi, "Soft robotics technologies to address shortcomings in today's minimally invasive surgery: The STIFF-FLOP approach," *Soft Robot.*, vol. 1, no. 2, pp. 122–131, 2014.

[20] A. Slatkin, J. Burdick, and W. Grundfest, *The Development of a Robotic Endoscope Experimental Robotics IV*, vol. 223, O. Khatib and J. Salisbury, Eds., Berlin, Germany: Springer, 1997, pp. 161–169.

[21] L. Phee, D. Accoto, A. Menciassi, C. Stefanini, M. C. Carrozza, and P. Dario, "Analysis and development of locomotion devices for the gastrointestinal tract," *IEEE Trans. Biomed. Eng.*, vol. 49, no. 6, pp. 613–616, Jun. 2002.

[22] M. Mahvash and P. E. Dupont, "Stiffness control of surgical continuum manipulators," *IEEE Trans. Robot.*, vol. 27, no. 2, pp. 334–345, Apr. 2011.

[23] R. E. Goldman, A. Bajo, and N. Simaan, "Compliant motion control for multisegment continuum robots with actuation force sensing," *IEEE Trans. Robot.*, vol. 30, no. 4, pp. 890–902, Aug. 2014.

[24] Y.-J. Kim, S. Cheng, S. Kim, and K. Iagnemma, "A novel layer jamming mechanism with tunable stiffness capability for minimally invasive surgery," *IEEE Trans. Robot.*, vol. 29, no. 4, pp. 1031–1042, Aug. 2013.

[25] Y.-J. Kim, S. Cheng, S. Kim, and K. Iagnemma, "A stiffness-adjustable hyperredundant manipulator using a variable neutral-line mechanism for minimally invasive surgery," *IEEE Trans. Robot.*, vol. 30, no. 2, pp. 382–395, Apr. 2013.

[26] M. S. Moses, M. D. M. Kutzer, H. Ma, and A. Mehran, "A continuum manipulator made of interlocking fibers," in *Proc. IEEE Int. Conf. Robot. Autom.*, 2013, pp. 4008–4015.

[27] T. Ranzani, G. Gerboni, M. Cianchetti, and A. Menciassi, "A bioinspired soft manipulator for minimally invasive surgery," *Bioinspir. Biomim.*, vol. 10, p. 035008, 2015.

[28] M. Cianchetti, T. Ranzani, G. Gerboni, I. De Falco, C. Laschi, and A. Menciassi, "STIFF-FLOP surgical manipulator: Mechanical design and experimental characterization of the single module," in *Proc. IEEE/RSJ Int. Conf. Intell. Robots Syst.*, 2013, pp. 3576–3581.

[29] K. Harada, D. Oetomoa, E. Susilo, A. Menciassia, D. Daneya, J.-P. Merleta, and P. Dario, "A reconfigurable modular robotic endoluminal surgical system: Vision and preliminary results," *Robotica*, vol. 28, no. 02, pp. 171–183, 2010.

[30] (2015, Oct.). [Online]. Available: http://www.stiff-flop.eu/

[31] M. Zimmermann, T. Ranzani, A. Menciassi, and B. Kellner, "Development of a cable actuated joint for a surgical robotic flexible arm," *Biomed. Eng.*, vol. 58, no. SI-1, 2013.

[32] S. Yi, S. S. Yun, and J. Paik, "Characterization of silicone rubber based soft pneumatic actuators," in *Proc. IEEE/RSJ Int. Conf. Intell. Robots Syst.*, Nov. 2013, pp. 4446–4453.

[33] A. De Greef, P. Lambert, and A. Delchambre, "Towards flexible medical instruments: Review of flexible fluidic actuators," *Precision Eng.*, vol. 33, pp. 311–321, 2009.

[34] O. H. Yeoh and P. D. Fleming, "A new attempt to reconcile the statistical and phenomenological theories of rubber elasticity," *J. Polymer Sci. B, Polymer Phys. Ed.*, vol. 35, no. 12, pp. 1919–1932, 1997.

[35] K. Suzumori, S. Endo, T. Kanda, N. Kato, and H. Suzuki, "A bending pneumatic rubber actuator realizing soft-bodied manta swimming robot," in *Proc. IEEE Int. Conf. Robot. Autom.*, Apr. 10–14, 2007, pp. 4975–4980.

[36] Y. Elsayed, A. Vincenzi, C. Lekakou, T. Geng, C. Saaj, T. Ranzani, M. Cianchetti, and A. Menciassi, "Finite element analysis (FEA) and design optimization of a pneumatically actuating silicone module for robotic surgery applications," *Soft Robot.*, vols. 1–4, no. 2014, pp. 255–262, 2014.

[37] F. Llievski, A. D. Mazzeo, R. F. Shepherd, X. Chen, and G. M. Whitesides, "Soft robotics for chemists," *Angew. Chem.*, vol. 123, pp. 1930–1935, 2011.

[38] B. Chang, A. Chew, N. Naghshineh, and C. Menon, "A spatial bending fluidic actuator: Fabrication and quasi-static characteristics," *Smart Mater. Struct.*, vol. 21, no. 4, p. 045008, 2012.

[39] K. Galloway, P. Polygerinos, C. Walsh, and R. J. Wood, "Mechanically programmable bend radius for fiber-reinforced soft actuators," presented at the Int. Conf. Adv. Robot., Montevideo, Uruguay, Nov. 2013.

[40] Y. Shapiro, A. Wolf, and K. Gabor, "Bi-bellows: Pneumatic bending actuator," *Sens. Actuators A, Phys.*, vol. 167, no. 2, pp. 484–494, 2011.

[41] D. G. Caldwell, G. A. Medrano-Cerda, and M. Goodwin, "Control of pneumatic muscle actuators," *IEEE Control Syst.*, vol. 15, no. 1, pp. 40–48, Feb. 1995.

[42] K. Suzumori, S. Wakimoto, K. Miyoshi, and K. Iwata, "Long bending rubber mechanism combined contracting and extending fluidic actuators," in *Proc. IEEE/RSJ Int. Conf. Intell. Robots Syst.*, Nov. 2013, pp. 4454–4459.

[43] T. Moers and D. Reynaerts, "Hydraulic actuation in miniature medical robots," presented at the EUSPEN Int. Conf., San Sebastian, Spain, Jun. 2–5, 2009.

[44] T. Manwell, T. Vítek, T. Ranzani, A. Menciassi, K. Althoefer, and H. Liu, "Elastic mesh braided worm robot for locomotive endoscopy," in *Proc. 36th Annu. Int. Conf. IEEE Eng. Med. Biol. Soc.*, pp. 848–851, Aug. 2014.

[45] A. Loeve, P. Breedveld, and J. Dankelman, "Scopes too flexible . . . and too stiff," *IEEE Pulse*, vol. 1, no. 3, pp. 26–41, Nov./Dec. 2010.

[46] L. S. Cowan and I. D. Walker, "The importance of continuous and discrete elements in continuum robots," *Int. J. Adv. Robot. Syst.*, vol. 10, art. 165, 2013.

[47] A. J. Liu and S. R. Nagel, "Jamming is not just cool anymore," *Nature*, vol. 396, pp. 21–22, 1998.

[48] J. R. Amend, E. M. Brown, N. Rodenberg, H. M. Jaeger, and H. Lipson, "A positive pressure universal gripper based on the jamming of granular material," *IEEE Trans. Robot.*, vol. 28, no. 2, pp. 341–350, Apr. 2012.

[49] A. Jiang, T. Ranzani, G. Gerboni, L. Lekstutyte, K. Althoefer, P. Dasgupta, and T. Nanayakkara, "Robotic granular jamming: Does the membrane matter?" *Soft Robot.*, vol. 1, no. 3, pp. 192–201, 2014.

[50] N. G. Cheng, M. B. Lobovsky, S. J. Keating, A. M. Setapen, K. I. Gero, A. E. Hosoi, and K. D. Lagnemma, "Design and analysis of a robust, low-cost, highly articulated manipulator enabled by jamming of granular media," in *Proc. IEEE Int. Conf. Robot. Autom.*, May 2012, pp. 4328–4333.

[51] E. Steltz, A. Mozeika, J. Rembisz, N. Corson, and H. Jaeger, "Jamming as an enabling technology for soft robotics," *Proc. SPIE*, vol. 7642, p. 63, 2010.

[52] A. Loeve, O. S. van de Ven, J.G. Vogel, P. Breedveld, and J. Dankelman, "Vacuum packed particles as flexible endoscope guides with controllable rigidity," *Granular Matter*, vol. 12, pp. 543–554, 2010.

[53] A. Jiang, A. Ataollahi, K. Althoefer, P. Dasgupta, and T. Nanayakkara, "A variable stiffness joint by granular jamming," in *Proc. Proc. Int. Design Eng. Tech. Conf. Comput. Inf. Eng. Conf.*, Aug. 2012, pp. 267–275.

[54] M. Li, T. Ranzani, S. Sareh, L. Seneviratne, P. Dasgupta, H. Wurdemann, and K. Althoefer, "Multi-fingered haptic palpation utilizing granular jamming stiffness feedback actuators," *Smart Mater. Struct.*, vol. 23, no. 9, p. 095007, 2014.

[55] R. J. Webster III and B. A. Jones, "Design and kinematic modeling of constant curvature continuum robots: A review," *Int. J. Robot. Res.*, vol. 29, no. 13, pp. 1661–1683, 2010.

[56] K. Suzumori, S. Iikura, and H. Tanaka, "Flexible microactuator for miniature robots," in *Proc. IEEE Micro Electro Mechanical Syst.*, 1991, string pp. 204–209.

[57] X. Wang, T. Geng, Y. Elsayed, T. Ranzani, C. Saaj, and C. Lekakou, "A new coefficient-adaptive orthonormal basis function model structure for identifying a class of pneumatic soft actuators," in *Proc. IEEE/RSJ Int. Conf. Intell. Robots Syst.*, Sep. 2014, pp. 530–535.

[58] J. Fraś, J. Czarnowski, M. Maciaś, and J. Główka, "Static modeling of multisection soft continuum manipulator for stiff-flop project," in *Recent Advances in Automation, Robotics and Measuring Techniques* (ser. Advances in Intelligent Systems and Computing), vol. 267. New York, NY, USA: Springer, 2014, pp. 365–375.

[59] G. Gerboni, T. Ranzani, A. Diodato, G. Ciuti, M. Cianchetti, and A. Menciassi, "Modular soft mechatronic manipulator for minimally invasive surgery (MIS): Overall architecture and development of a full integrated soft module," *Meccanica*, vol. 50, no. 11, pp. 2865–2878, 2015.

[60] T. C. Searle, K. Althoefer, L. Seneviratne, and H. Liu, "An optical curvature sensor for flexible manipulators," in *Proc. IEEE Int. Conf. Robot. Autom.*, May 2013, pp. 4415–4420.

[61] Y. Noh, S. Sareh, J. Back, H. A. Wurdemann, T. Ranzani, E.-L. Secco, A. Faragasso, H. Liu, and K. Althoefer, "A three-axial body force sensor for flexible manipulators," in *Proc. IEEE Int. Conf. Robot. Autom.*, May 2013, pp. 6388–6393.

[62] S. Sareh, A. Jiang, A. Faragasso, Y. Noh, T. Nanayakkara, P. Dasgupta, L. Seneviratne, H. A. Wurdemann, and K. Althoefer, "Bio-inspired tactile sensor sleeve for surgical soft manipulators," in *Proc. IEEE Int. Conf. Robot. Autom.*, May 2014, pp. 1454–1459.

[63] Y. Elsayed, C. Lekakou, T. Ranzani, M. Morino, A. Arezzo, A. Menciassi, T. Geng, and C. Saaj, "Crimped braided sleeves for soft, actuating arm in robotic abdominal surgery," *Minimally Invasive Therapy Allied Technol.*, vol. 24, no. 4, pp. 204–210, 2014.

Tommaso Ranzani received the B.E. and M.E. degrees in biomedical engineering from The University of Pisa, Pisa, Italy, in 2008 and 2010, respectively, and the Ph.D. degree in biorobotics from The Biorobotics Institute of the Scuola Superiore Sant'Anna, Pisa, in 2014.

Since 2014, he has been a Postdoctoral Fellow with the Harvard John A. Paulson School of Engineering and Applied Science, Cambridge, MA, USA. His research interests include medical and surgical robotics, soft robotics, and advanced manufacturing.

Matteo Cianchetti (M'05) received the Master's (Hons.) degree in biomedical engineering from The University of Pisa, Pisa, Italy, in July 2007 and the Ph.D. (Hons.) degree in biorobotics from the Biorobotics Institute of the Scuola Superiore Sant'Anna, Pisa.

He is currently an Assistant Professor with the Biorobotics Institute, leading the Soft Mechatronics for Biorobotics Laboratory, and he is author or coauthor of more than 50 international peer-reviewed papers He regularly serves as a reviewer for more than 10 international ISI journals. He has been and currently is involved in EU-funded projects with the main focus on the development of soft robotics technologies. His main research interests include bioinspired robotics and the study and development of new systems and technologies based on soft/flexible materials for soft actuators, smart compliant sensors, and flexible mechanisms.

Dr. Cianchetti is a Member of the IEEE Engineering in Medicine and Biology and Robotics and Automation Society.

Giada Gerboni (M'10) received the B.E. and M.E. degrees in biomedical engineering from the Department of Engineering, The University of Pisa, Pisa, Italy, in 2009 and 2011, respectively, and the Ph.D. (Hons.) degree in biorobotics from the Biorobotics Institute, Scuola Superiore Sant'Anna, Pisa.

She was a Visiting Research Fellow with the Biomechanical Department, TU Delft, The Netherlands, with the Bio-Inspired Technology (BITE) group. Her research interests include the mechanical design of medical instruments, medical robotics, bio-inspired design, development of innovative actuation/sensing mechanisms, and soft robotics.

Iris De Falco was born in Italy in 1987. She received the Master's degree *(cum laude)* in biomedical engineering from The University of Pisa, Pisa, Italy, in February 2012. She is currently working toward the Ph.D. degree in biorobotics at the Biorobotics Institute, Scuola Superiore Sant'Anna, Pisa, Italy, focusing on innovative actuation and sensing mechanisms for minimally invasive robotic surgery.

She was a Visiting Researcher with Department of BioMechanical Engineering, TU Delft, The Netherlands, in 2015. Her main research interests include design of medical instruments, bio-inspired robots, and soft robotics.

Arianna Menciassi (M'00–SM'15) received the Master's degree in physics (Hons.) from University of Pisa, Pisa, Italy, and the Ph.D. degree in bioengineering from Scuola Superiore Sant'Anna, Italy, in 1995 and 1999, respectively.

She is currently a Full Professor with the BioRobotics Institute, Scuola Superiore Sant'Anna, and she is Area Leader of "Surgical Robotics and Allied Technologies."

She has intense research and training activity at a high level (master degree candidates in biomedical engineering, Ph.D. degree students, etc.). Her main research interests include biomedical robotics, surgical robotics, microsystem technology, nanotechnology with special attention to the synergy between robot-assisted therapy, and micro/nanotechnology-related solutions. She is the co-author of more than 330 scientific publications (more than 200 in ISI journals) and 6 book chapters on biomedical robots/devices and microtechnology.

She served on the Editorial Board of IEEE-ASME TRANSACTIONS ON MECHATRONICS and she is currently the Topic Editor in Medical Robotics for *International Journal of Advanced Robotic Systems*. She is the co-chair of the IEEE-RAS Technical Committee on Surgical Robotics. She is involved in the BioRobotics Technical Committee of IEEE-EMBC.